Climate Dynamics (2026) 64:421
https://doi.org/10.1007/s00382-026-08372-0

A hot-flood teleconnection as a key contributor to the extreme April 2024 precipitation in Guangdong

Yina Diao[1] · Xinning Zhang[1,3] · Jianping Li[1,2] · Yinan Yang[1] · Yazhou Zhang[1] · Fei Huang[1] · Zhaolu Hou[1]

Received: 7 December 2025 / Accepted: 25 August 2026

Abstract

Guangdong experienced extreme precipitation in April 2024, marking the highest April precipitation since 1951. Using perturbation potential energy (PPE) as a diagnostic perspective, this study reveals that the event can be attributed to the extremeness of the remote extreme heat over Eastern Europe and the local transition of PPE to kinetic energy. The extreme temperature anomaly over Eastern Europe is accompanied by anomalously Eastern Europe high PPE (EEPPE), which acts as a stable wave source that strengthens and sustains the Eastern Europe high -West Asia low (EEWA) wave train. The EEWA wave train affects the thermodynamic environment in Guangdong through two pathways: by modulating the upper troposphere westerly jet along south of the West Asia low to influence vertical motion, and by modulating local thermal advection to alter the PPE. Therefore, the increase of the EEPPE is accompanied by enhanced vertical velocity and PPE over Guangdong. The enhanced upward motion further facilitates the conversion of local PPE to kinetic energy which intensifies precipitation. These mechanisms establish a dynamical link between heat extremes in Eastern Europe and flooding in Guangdong. The PPE anomalies over Eastern Europe can serve as a one-week precursor to precipitation in Guangdong. This connection is not unique to April 2024; it has persisted since the early twenty-first century. However, in April 2024, the prolonged extreme heat in Europe contributes to the long-lasting extreme precipitation in Guangdong.

Keywords Extreme precipitation · Atmospheric perturbation potential energy (PPE) · Hot-flood teleconnection · Eastern Europe · PPE-kinetic energy transition

1 Introduction

Guangdong Province lies in South China, northwest of the South China Sea, and is located in the East Asian monsoon region. The rainy season in South China lasts from April to September (Ding 1992; Gao et al. 2017) and can be divided into two periods: the first rainy season (April to June) and the second rainy season (July to September) (Ma et al. 2018; Ding and Wang 2008; Gu et al. 2018; Fang et al. 2012). The first rainy season in South China can be further divided into the pre- and post-monsoon onset periods (Jiang et al. 2017; Chen and Luo 2018). Since the climatological outbreak of the South China Sea summer monsoon occurs in May (Xie et al. 1998; Wang et al. 2004; Ding and Wang 2008; Luo et al. 2013), the April precipitation concerned in this study belongs to the pre-monsoon period.

During this specific pre-monsoon period in April, the tropical monsoon circulation has not yet fully established over South China. Consequently, the precipitation in this region is profoundly modulated by the mid-to-high latitude atmospheric circulations. Specifically, the upper troposphere over the Eurasian continent is dominated by the subpolar and subtropical westerly jets, which originate from Europe and extend eastward across the continent. When encountering the Qinghai-Tibet Plateau, the subtropical jet

✉ Jianping Li
ljp@ouc.edu.cn

✉ Yazhou Zhang
zyz@ouc.edu.cn

1 Frontiers Science Center for Deep Ocean Multispheres and Earth System (FDOMES)/Key Laboratory of Physical Oceanography/Academy of the Future Ocean/College of Oceanic and Atmospheric Science, Ocean University of China, Qingdao, China

2 Laboratory for Ocean Dynamics and Climate, Qingdao Marine Science and Technology Center, Qingdao 266237, China

3 Hebei Meteorological Observatory, 050021 Shijiazhuang, China

is further split into northern and southern branches. These westerly jets act as crucial waveguides for the propagation of multi-scale Rossby waves. Located at the southeast coast of the Eurasian continent, Guangdong Province lies directly downstream of these westerly jets. As a result, Rossby waves and lower-tropospheric synoptic cyclones travel southeastward along these jet waveguides, bringing cold air to South China (Li et al. 2024). When the intruding cold air encounters the warm and moist air from the south, frontal precipitation is triggered. Thus, the rainfall in South China during this period is predominantly characterized by frontal precipitation (Chi et al. 2005; Yuan et al. 2010). Previous studies have shown that this pre-monsoon precipitation can be significantly influenced by remote features, such as anomalous snow cover in Europe, western Siberia, or the Lake Baikal region, as well as upstream air-sea coupled systems like the North Atlantic Oscillation (Wu and Kirtman 2007; Shao and Zhang 2012; Zuo et al. 2012; Jia et al. 2018; Xiao et al. 2025). Therefore, during April–May, the precipitation variability in South China is largely dominated by a 10–20-day oscillation (Qiu et al. 2022; Miao et al. 2019), an intraseasonal time scale closely connected with mid-latitude planetary-scale adjustments.

Located near the Tropic of Cancer, the pre-monsoon precipitation in Guangdong is found to be also connected with the tropical circulation systems. Abundant moisture is transported from South China Sea to South China by tropical circulation systems such as the Western Pacific Subtropical High and the MJO (Ding 1994), which is a factor responsible for the heavy rains in the pre-monsoon-onset period. Moreover, SST anomalies over the Indian Ocean and Western tropical Pacific can influence South China precipitation through their impacts on the above-mentioned tropical circulation systems (Yang and Lau 2004; Wan et al. 2009; Xu et al. 2019; Bai et al. 2011).

Though the major extreme heavy rains occur in monsoon season, heavy rains over South China before the onset of the South China Sea summer monsoon are also found to occur under the following conditions (Wang et al. 2014a; Huang et al. 2019). Prolonged heavy rains occur when both warm and cold air are of comparable intensity in which wind field exhibits a shear line near South China. The wet phase of MJO disturbance plays a crucial role in transport and convergence of moisture over South China (Chen et al. 2015, 2016). Coastal heavy rains in South China are often shown as the warm-sector rains, majority of which are accompanied by a low-level jet (Zhang and Meng 2019) and associated with mesoscale convective systems (Luo et al. 2013; Wang et al. 2014a; Wu and Luo 2016).

In April 2024, Guangdong Province experienced extreme precipitation events. The monthly rainfall broke the historical record for April since 1951(Fig. 1c). Persistent extreme precipitation events occurring in northern Guangdong, leading to severe disasters. Recently, Zhang et al. (2025) discussed the cause of this April extreme precipitation in Guangdong. They found that joint effects of the MJO events and the anti-cyclonic circulation over the western North Pacific (ACC) that is maintained by warm western tropical Indian Ocean SST which is induced by co-occurrence of El Niño and positive Indian Ocean Dipole events enhanced northward water vapor transport thus contribute to extreme April precipitation in Guangdong. Enhanced warm and moisture air transported by the ACC did play a critical role in the occurrence of extreme precipitation. However, this April precipitation occurs mainly over north of Guangdong (Fig. 1a) and exhibits as frontal rainfalls. In frontal rain cases, warm air rises over cold air or is induced by low level convergence over cyclonic shearing line, and upper-level divergence and cold air transport are also critical factors for frontal air rising, which are usually connected with upper-level westerly jet exit zone and zonal wave induced northerly winds. Moreover, this April precipitation in Guangdong show a multi-time scale variabilities of both synoptical transient (2–7 days) and planetary scale modulation scale (longer than two weeks). So, mid-latitude large scale waves should be another important side other than the warm air transport. We also notice an important feature in this April extreme precipitation that, 2024 was the warmest year in a multi-dataset record of global temperature going back to 1850 (https://climate.copernicus.eu/global-climate-highlights-2024). The hottest region in the Eurasian continent in April was over the Eastern Europe and Southeast Asia, where the April 2m air temperature was recorded as the Rank 1st hottest in the period 1951–2024 (Fig. 1c). Does the highest temperature in Eastern Europe and Southeast Asia is connected with the extreme precipitation in Guangdong? And how the two distinct climate anomalies are connected with each other?

Previous studies usually investigate the remote influence or the teleconnection through correlation analysis in the geopotential, temperature or velocity fields. To dig deeply the physical connection between the remote high air temperature and precipitation in Guangdong, we use a tool of the perturbation potential energy (PPE), which is proposed by Li and Gao (2006). The PPE represents the maximum value of local total potential energy that can be converted into kinetic energy. Notably, the coupling between PPE and kinetic energy is stronger than that between traditional available potential energy (APE) (Lorenz 1955) and kinetic energy. In most continental regions, the PPE is critically determined by air temperature that is mainly influenced by atmosphere circulation (Gao and Li 2013; Wang et al. 2014b, 2015). While over sea surface, especially in tropical, apparent heat source plays an essential role in the PPE

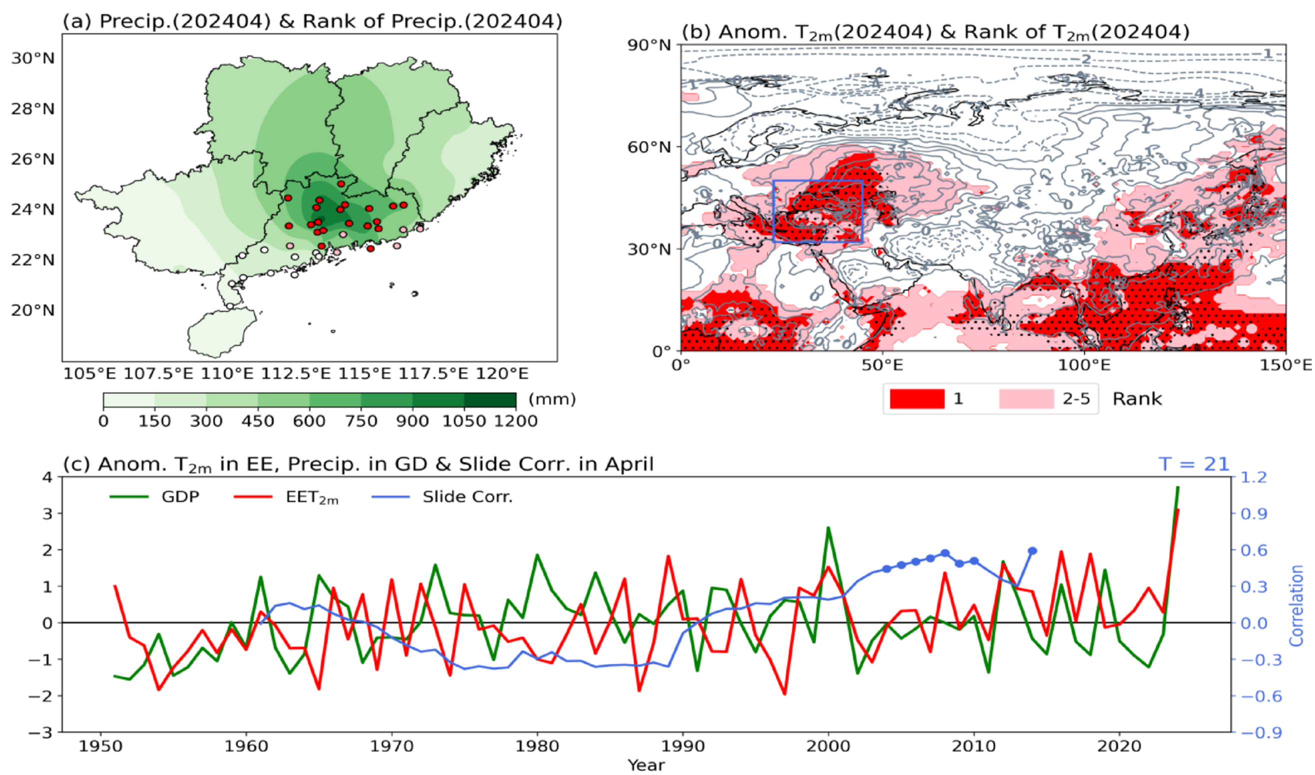

Fig. 1 **a** Spatial distribution of April precipitation (green shading, mm, interpolated from station data) in Guangdong and the surrounding provinces, along with the rankings of precipitation in Guangdong (red solid dots), **b** 2m air temperature anomalies (contours, °C) and the rankings (red shading) in April 2024, in which the ranking denotes the sort in period 1951–2024 and the solid black points denote the above 99% confidence levels; and **c** the normalized indices of the Eastern Europe 2m air temperature (EET_{2m}, the temperature averaging over the Eastern Europe enclosed by the blue rectangle in (**b**), red line), Guangdong precipitation (GDP, green line) and the 21-year running correlation coefficients (blue line) between them, in which the solid blue points denote the above 95% confidence levels

(Gao and Li 2013). The tool of PPE has been successfully applied to studies of regional climate variability (Huyan et al. 2017; Zhang et al. 2019, 2023). In this study, we trace the temporal-spatial variabilities of the PPE and its transition, and the variabilities of circulations accompanying the energy changes to find how the remote Eastern Europe high temperature is connected with precipitation in Guangdong to shape a hot-flood teleconnection.

The remainder of the article is organized as follows. Section 2 introduces the data and methods employed in this study. Results are show in Sect. 3, in which Sect. 3.1 shows the extremeness of Guangdong April precipitation, the remote connection illustrated by large scale backgrounds is discussed in Sect. 3.2, how the Eastern Europe high PPE influences Guangdong extreme precipitation through the EEWA wave train is investigated in Sect. 3.3, the connection between the local PPE release and the extreme precipitation is discussed in Sect. 3.4. Section 4 provides the conclusions and a summary.

2 Data and method

2.1 Data

Precipitation is based on the in-situ rainfall observations from the National Meteorological Information Center of China to analyze. The ERA5 reanalysis dataset from the European Centre for Medium-Range Weather Forecasts (ECMWF; Hersbach et al. 2023) provides the hourly, daily and monthly reanalysis variables, including 2m temperature, outgoing longwave radiation (OLR), multi-pressure-level temperature, vertical velocity, zonal and meridional wind components, geopotential height and specific humidity. The original 0.25°×0.25° grid resolution is interpolated to 1°×1°. All the data cover the period 1951–2024, and the April anomaly is obtained by excluding the climatological mean of 1991–2020, with the exception of the 2m temperature and precipitation series in Fig. 1c, which instead use the climatological mean of 1951–2024. The MJO index used in this study is the OLR-based MJO Index (OMI) from the National Oceanic and Atmospheric Administration (NOAA), with daily temporal resolution.

2.2 Methods

2.2.1 PPE and its governing equation

We use the perturbation potential energy (PPE) theory (Li and Gao 2006) to analyze extreme precipitation events. The complete expression of PPE takes the form of a series expansion, where higher-order moment terms exhibit significantly smaller magnitudes compared to lower-order terms and can therefore be neglected in local analyses. By averaging PPE globally, the average of PPE_1 is 0, and the average of PPE_2 corresponds to the available potential energy (APE; Lorenz 1955). Thus, the PPE_1 dominates the local energy availability, while the APE is the energy availability of the global atmospheric system. The PPE_1 is as follows:

$$PPE_1 = \frac{1}{\gamma_d} \int_0^{p_s} T' dp \tag{1}$$

where p and p_s are the pressure and surface pressure, respectively; $\gamma_d = g/c_p$ indicates the dry adiabatic lapse rate, where g is the gravitational acceleration and c_p is the specific heat at constant pressure; T' denotes the departure of temperature.

The governing equations of PPE_1 and perturbation kinetic energy (PKE) are as follows (Gao 2006; Zhang et al. 2019; Zhao et al. 2024):

$$\frac{\partial PPE_1}{\partial t} = PC_{pe} + G + HBF_{pe} \tag{2}$$

$$\frac{\partial PKE}{\partial t} = -PC_{pe} + D + HBF_{ke} \tag{3}$$

$$PC_{pe} = \frac{1}{g} \int_0^{p_s} \left(\omega\alpha - \overline{\omega\alpha}\right) dp \tag{4}$$

where PC_{pe} is the perturbation energy conversion between PPE_1 and PKE. The subscripts *pe* and *ke* denote terms associated with the perturbation potential energy and perturbation kinetic energy, respectively. ω is the pressure vertical velocity, and α is the specific volume. The overbar $(\overline{\omega\alpha})$ represents the global average on an isobaric surface. When $PC_{pe} < 0$, PPE_1 is converted to PKE. When $PC_{pe} > 0$, PKE is converted to PPE_1. G is the source (sink) term of atmospheric PPE_1 and depends on diabatic heating. D represents viscous dissipation. HBF_{pe} and HBF_{ke} represent the horizontal boundary fluxes PPE_1 and PKE, respectively. In this paper, PPE_1 is used to represent PPE for the analysis.

2.2.2 Rossby wave ray tracing and Rossby wave ray flux

We employ the Rossby wave ray tracing theory in a horizontally non-uniform basic flow (Li and Li 2012; Li et al. 2015, 2019; Zhao et al. 2015, 2019) to show Rossby wave propagation. Based on the previous theory, the dispersion relationship of the Rossby wave frequency and wavenumber in a horizontally non-uniform flow can be written as (Karoly 1983; Li and Nathan 1997):

$$\sigma = \overline{u}_M k + \overline{v}_M l + \frac{\overline{q}_x l - \overline{q}_y k}{k^2 + l^2} \tag{5}$$

where σ is the wave frequency; k and are the zonal and meridional wavenumbers, respectively; $(\overline{u}_M, \overline{v}_M) = (\overline{u}, \overline{v}) / \cos\varphi$ is the Mercator projection of zonal and meridional winds; φ is latitude; $\overline{q} = \nabla_M^2 \overline{\psi} / \cos^2\varphi + f$ is the absolute vorticity of the background; $\overline{q}_x$ and $\overline{q}_y$ are the zonal and meridional gradients of $\overline{q}$; $K^2 = \sqrt{k^2 + l^2}$ is the total wave number, and the zonal and meridional components of the group velocity take the form as:

$$u_g = \frac{\partial\sigma}{\partial k} = \overline{u}_M + \frac{\left(k^2 - l^2\right)\overline{q}_y - 2kl\overline{q}_x}{K^4} \tag{6a}$$

$$v_g = \frac{\partial\sigma}{\partial l} = \overline{v}_M + \frac{\left(k^2 - l^2\right)\overline{q}_x + 2kl\overline{q}_y}{K^4} \tag{6b}$$

When the background flow changes along the ray, wavenumbers determined from the kinematic wave theory can be expressed as follows (Whitham 1960):

$$\frac{d_g k}{dt} = -\frac{\partial\sigma}{\partial x} = -k\frac{\partial\overline{u}_M}{\partial x} - l\frac{\partial\overline{v}_M}{\partial x} - \frac{1}{K^2}\left(l\frac{\partial\overline{q}_x}{\partial x} - k\frac{\partial\overline{q}_y}{\partial x}\right) \tag{7a}$$

$$\frac{d_g l}{dt} = -\frac{\partial\sigma}{\partial y} = -k\frac{\partial\overline{u}_M}{\partial y} - l\frac{\partial\overline{v}_M}{\partial y} - \frac{1}{K^2}\left(l\frac{\partial\overline{q}_x}{\partial y} - k\frac{\partial\overline{q}_y}{\partial y}\right) \tag{7b}$$

Equations (6) and (7) collectively form a complete wave ray tracing equation set. Given a starting point and an initial zonal wave number k, the corresponding local meridional wave number is determined by the dispersion relation (Eq. 5). By numerically integrating these equations, the Rossby wave ray trajectory can be obtained. The integrations were terminated to omit the small-scale Rossby waves once the local meridional wave length was less than 1000 km.

Building upon the Rossby wave ray tracing theories in horizontally nonuniform basic flows mentioned above, Yang and Li (2025) introduce a new concept of horizontal Rossby wave ray flux (Li-Yang WRF) to diagnose local activity and propagation direction of Rossby waves. It represents the flow amount of wave rays passing through a unit grid area per unit time as follows:

$$F_{WR} = \frac{1}{S_\varphi}\iint_{S_\varphi} V_R dS_\varphi = (u_R i + v_R j) \tag{8}$$

$$u_R = \sum_{i=1}^{n} a\cos\varphi_i \frac{\Delta\lambda_{Ri}}{\Delta t} \tag{9}$$

$$v_R = \sum_{i=1}^{n} a\frac{\Delta\varphi_{Ri}}{\Delta t} \tag{10}$$

where S_φ is the area element of the grid integral, a is the radius of the earth, φ is the latitude, $\Delta\lambda_{Ri}$. and $\Delta\varphi_{Ri}$ $(i = 1, 2, \ldots, n)$ represent the longitude and latitude distances of the wave ray trajectory passing through the given small grid, Δt represents the duration of the period for the ray passing through the given small grid. The unit of the Li-Yang WRF is m s^{-1}. The magnitude of the Li-Yang WRF denotes the strength of local Rossby wave activity, while its vectors indicate the direction of wave propagation. The Li-Yang WRF provides a clearer and more precise depiction of wave activity strength and propagation direction in a vectorial form.

In this study, the local activity and propagation direction of Rossby waves are diagnosed using the Li-Yang WRF rather than traditional methods such as the Eliassen–Palm (E–P) flux (Eliassen and Palm 1961; Andrews and McIntyre 1976; Edmon et al. 1980; Trenberth 1986), Plumb wave activity flux (Plumb 1985), and Takaya–Nakamura (T–N) wave activity flux (Takaya and Nakamura 2001). This choice is motivated by two critical limitations of conventional fluxes. First, while traditional methods effectively measure overall wave magnitude and direction within a region, they cannot isolate signals originating from specific wave sources. Because multiple excitation points can simultaneously contribute to the target area, using these fluxes complicates the causal analysis of interacting phenomena. Second, traditional methods tend to increase rapidly in the tropics due to the small Coriolis parameter there, making them generally unsuitable for analyzing tropical Rossby waves. In contrast, the Li-Yang WRF overcomes these constraints by bridging the Lagrangian perspective (focusing on wave motion trajectories) (Lagrange 1853) and the Eulerian perspective (quantifying local wave intensity) (Euler 1757). The unique advantage of the Li-Yang WRF is its ability to effectively represent influential waves strictly from a certain wave source, leaving relatively unrelated wave components distinguishable. By avoiding tropical distortions and isolating specific wave pathways, the Li-Yang WRF appears as a concentrated flux with a coherent overall direction, thereby ensuring the robustness and causal clarity of the identified wave train paths in our analysis (Yang et al. 2025).

2.2.3 Ranking attribution method (RAM)

Previous studies on individual extreme climate events have consistently demonstrated that extreme events are typically driven by extreme controlling factors. For instance, the strongest Australian High on record triggered the record-breaking rainfall over South China in June 2017 (Sun et al. 2018); the record-breaking northward shift of the Western Pacific Subtropical High led to the unprecedented 2018 Northeast Asia heatwave (Ren et al. 2020); and the unprecedented melting of Barents Sea ice triggered severe heatwaves in North America (Wei et al. 2024). Building on this premise, the Ranking Attribution Method (RAM) was proposed based on two core hypotheses (Sun et al. 2023). The first hypothesis is the physical basis: extreme events are intrinsically linked to extreme forcings. Thus, it is physically sound and feasible to identify potential drivers based on their historical extremity, which is quantitatively reflected by their ranked positions. The second hypothesis highlights the statistical perspective of RAM: if a genuine causal relationship exists between two physical variables, they may or may not exhibit a long-term linear correlation. The absence of a strong linear correlation often points to the influence of sudden, nonlinear, or infrequently occurring extreme factors. By focusing strictly on historical extreme rankings, RAM provides a powerful diagnostic approach to effectively capture these sudden extreme forcings that might not be prominently reflected in long-term linear correlation analyses.

In practice, for a given extreme event occurring in a specific year, RAM evaluates potential drivers by calculating their ranked positions within the complete historical record. Positive ranks (1 denotes the historical maximum) indicate descending order, and negative ranks (−1 denotes the historical minimum) indicate ascending order. By filtering potential extreme variables based on these rankings and subsequently confirming the drivers through detailed physical and dynamic diagnostics, RAM provides a highly reasonable and easily comprehensible framework for extreme event attribution (Sun et al. 2023).

3 Results

3.1 Extremeness of Guangdong April precipitation

In April 2024, Guangdong Province experienced extreme precipitation. Generally, the April extreme precipitation showed two intense rainfall periods (P1: March 22 to April

8, and P2: April 17 to April 30) including four main extreme precipitation events (Fig. 3). The average precipitation across the province exceeded 500 mm, nearly three times the climatic average of 172 mm for April and the highest recorded since observations began in 1951. Maximum precipitation occurred in the north and central of Guangdong. We ranked the April precipitation data from 1951 to 2024 for each station. In April 2024, the central and northeastern regions recorded their highest precipitation in 74 years, with the maximum single-station monthly precipitation reaching nearly 1200 mm (Fig. 1a). Additionally, the precipitation lasted for an extended period, with rainfall occurring on about 70% of the days in April. Northern Guangdong experienced frequent and successive extreme precipitation. This extreme rainfall event caused severe socioeconomic losses.

Meanwhile, 2024 was the warmest year in a multi-dataset record of global temperature going back to 1850 (https://climate.copernicus.eu/global-climate-highlights-2024). The hottest region in the Eurasian continent in April 2024 was over the Eastern Europe, Southeast Asia and Western tropical Pacific (Fig. 1b), where the 2m air temperature in April 2024 is ranked the hottest in the period 1951–2024. So, according to the RAM (Sun et al. 2023), the extreme Guangdong precipitation may attribute to the high temperature in the Eastern Europe, since both the April precipitation in Guangdong and air temperature in east Europe reach the maximum in 2024. Moreover, the 21-year sliding correlation between April 2m temperatures in Eastern Europe and precipitation in Guangdong from 1951 to 2024 shows a highly significant positive correlation since the late 1990s. However, it is worth noting that this teleconnection exhibits significant interannual instability prior to that (e.g., displaying opposite trends around 1990, as shown in Fig. 1c). This complexity is likely attributed to decadal shifts in mid-latitude background circulations and the competing effects of various climate forcings, a specific topic deferred to our future work. Despite this past instability, the recent decadal background firmly establishes the connection between European temperature and Guangdong precipitation, implying that the European extreme heat in 2024 may dynamically induce the downstream extreme precipitation. Furthermore, this remote dynamic linkage is highly seasonally dependent, primarily limited to the pre-monsoon period (April). During April, the southward-positioned subtropical westerly jet provides a favorable waveguide for Rossby wave propagation. As the South China Sea summer monsoon erupts in May and June, this jet rapidly weakens and shifts northward (Ding 1992; Schiemann et al. 2009), substantially weakening the direct dynamic influence from mid-latitude wave trains as tropical systems take over (Luo et al. 2017; Chi et al. 2005). Therefore, focusing on this specific time window, how exactly are these two remote regions connected? How does the upstream extreme heat trigger the downstream precipitation far away? We will explore the specific dynamic wave propagation mechanisms in the following sections.

3.2 Remote connection illustrated by large scale backgrounds

The April mean 300 hPa geopotential height anomalies in 2024 show a stationary wave train from Europe to West Asia with high-low geopotential height anomaly centers at Eastern Europe and West Asia respectively (named as the EEWA wave train, hereafter), and the low pressure extends along north of the Qinghai-Tibet Plateau to southeast coast of China near Guangdong. The corresponding PPE anomalies show positive and negative values at Eastern Europe and West Asia respectively (Fig. 2a). We noted that the PPE anomalies over the Bay of Bengal and the Indo-China Peninsula are also positive. That is, the surrounding potential energy near Guangdong is also high but is much weaker compared with the strong positive PPE anomaly over the Eastern Europe. Therefore, across the Eurasian continent in April, the maximum PPE anomalies were located in Eastern Europe, which is highly consistent with the record-breaking 2m air temperatures observed in this region (Fig. 1b). The high ground surface temperature implies lower troposphere air is strongly heated which leads to an increase of horizontal air temperature gradient and an upward shift of local air column gravity center thus the increase of the PPE.

The high PPE in Eastern Europe can be considered as the source of Rossby waves. To further investigate the dynamic pathways, we calculated the April mean wave ray fluxes (Li-Yang WRF; Yang et al. 2025), along with the corresponding geopotential height and PPE anomalies (Fig. 2b). The calculated Li-Yang WRF vectors explicitly illustrate the spatial distribution and propagation of the wave energy. The Li-Yang WRF confirms that the wave energies originate from Eastern Europe and go southeastward to West Asia then go further eastward around the Qinghai-Tibet Plateau. The above results indicate that the low-pressure anomaly at West Asia and the high-pressure anomaly at Eastern Europe are connected by wave energy propagations thus constitutes a stationary wave train which also serves as a large-scale path of wave energy propagation from west to east. Therefore, the high temperature induced high PPE in Eastern Europe can influence the circulation near Guangdong through the wave train. Figure 2b further shows the mean time scale that the wave energy propagating from Eastern Europe to West Asia is nearly 3 days, to southeast China is nearly 6 days, and from West Asia to Southeast China is nearly 3–4 days.

The West Asia low pressure extends eastward to southeast China, south of which lies a strong monthly mean westerly jet (Fig. 2c). The jet core is located west of Indian

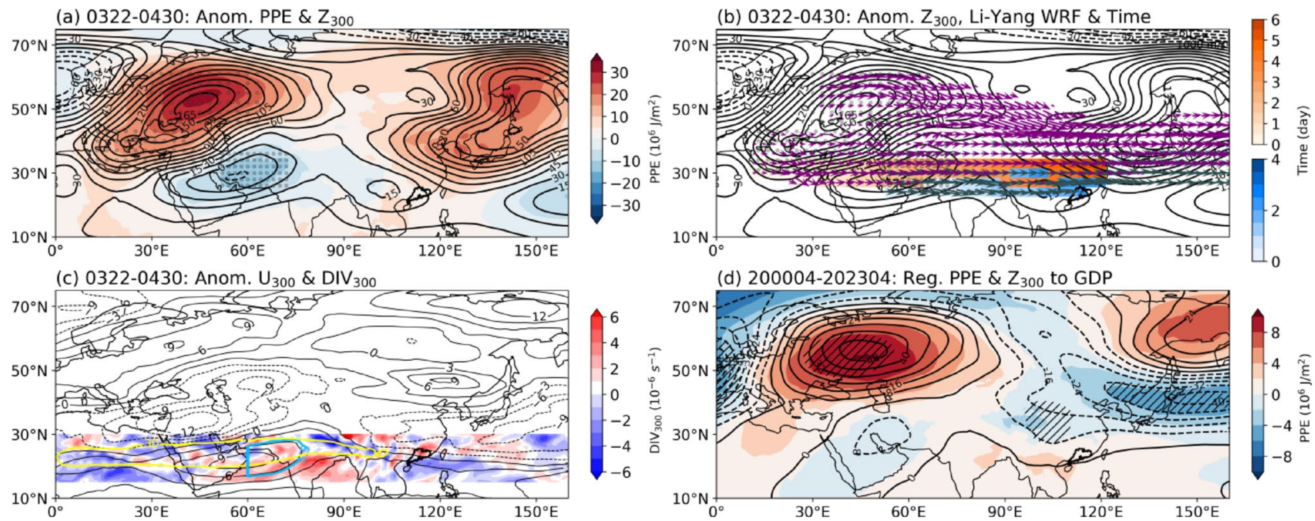

Fig. 2 **a** Anomalous PPE (shading, 10^6 J m^{-2}) and 300 hPa geopotential height (contours, gpm), **b** mean wave ray fluxes originate from Europe (purple vectors, m s^{-1}) and West Asia (green vectors, m s^{-1}), the time of wave energy propagating (shading, day), and 300 hPa geopotential height anomalies (contours, gpm) in which the gray dots denote the sources of the wave energy, **c** anomalous zonal wind (black contours, m s^{-1}) and its divergence (shading, 10^{-6} s^{-1}, shown only between 15° and 30°N) at 300 hPa, with the yellow contour indicating zonal wind speeds exceeding 30 m/s, and **d** regressions of the PPE and 300 hPa geopotential height anomalies to April Guangdong precipitation from 2000 to 2023, with the hatched area denoting above 95% confidential level

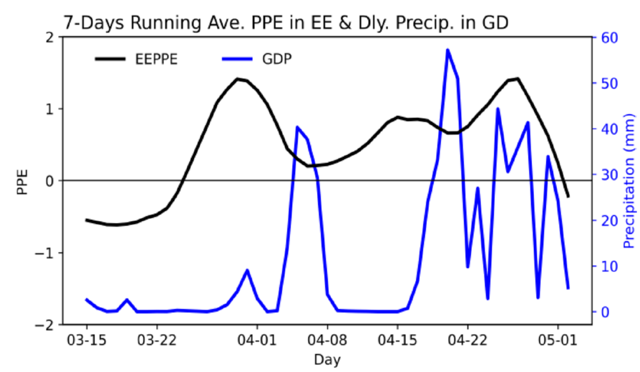

Fig. 3 Normalized 7-day running mean Eastern Europe PPE anomalies (EEPPE, black line) and daily Guangdong precipitation (GDP, blue line) from 15 March to 2 May 2024

Peninsula. So, the Guangdong Province is beneath the left of the jet-exit zone, where lies a strong jet induced divergence zone. The upper-level divergence leads to an strengthen of ascending which benefits the transition of local potential energy to kinetic energy (Zwack and Okossi 1986) that further accelerating the ascending. The left of jet-exit zone is also a region where a barotropic critical region may exist. It is a specific place where barotropic development is likely to occur and baroclinic instability is likely to be triggered (Rivière and Joly 2006a, 2006b). Therefore, it is a region that favors the intensification of low-level convergence and cyclonic circulation through the release of the potential energy. While, the intensity of this upper-level jet relies on the strength of the West Asia Low. So, a spatial connection between the Eastern Europe high PPE and the Guangdong precipitation forms.

Besides the primary EEWA pathway, Fig. 2b reveals that the wave ray fluxes bifurcate from Eastern Europe. A northern branch propagates eastward along the subpolar westerly jet, exciting a prominent anomalous anticyclone over the Sea of Japan. Located northeast of Guangdong, this anticyclone plays a crucial synergistic role in the extreme precipitation through downstream "blocking" and local "steering" effects. On the one hand, it acts as a downstream block that impedes the eastward progression of upstream synoptic systems, allowing the precipitation-favorable divergence field to persist over Guangdong for an extended duration. On the other hand, northeasterly flows at its southern flank steer mid-latitude cold air southwestward into South China, which triggers intense frontal convergence with tropical warm-moist air (Figs. 3, 4, 5, 6, and 7) and strengthens the low-level cyclonic lifting. Therefore, the synergistic interaction of both the northern and southern wave trains jointly orchestrated the extreme precipitation event in Guangdong in April 2024.

The above discussions indicate that the upstream wave trains (especially the EEWA) act as a bridge that connects the Eastern Europe high PPE and circulation corresponding to Guangdong extreme precipitation in April 2024. Is this decadal pattern only a random case or belongs to a long term climate variation? Since Fig. 1c shows that the April mean 2m air temperature has a significant positive correlation since the beginning of the twenty-first century, we regress the April mean 300 hPa geopotential height and the PPE anomalies to the GDP index in the period 2000–2023. The result (Fig. 2d) shows that the regressed circulation pattern

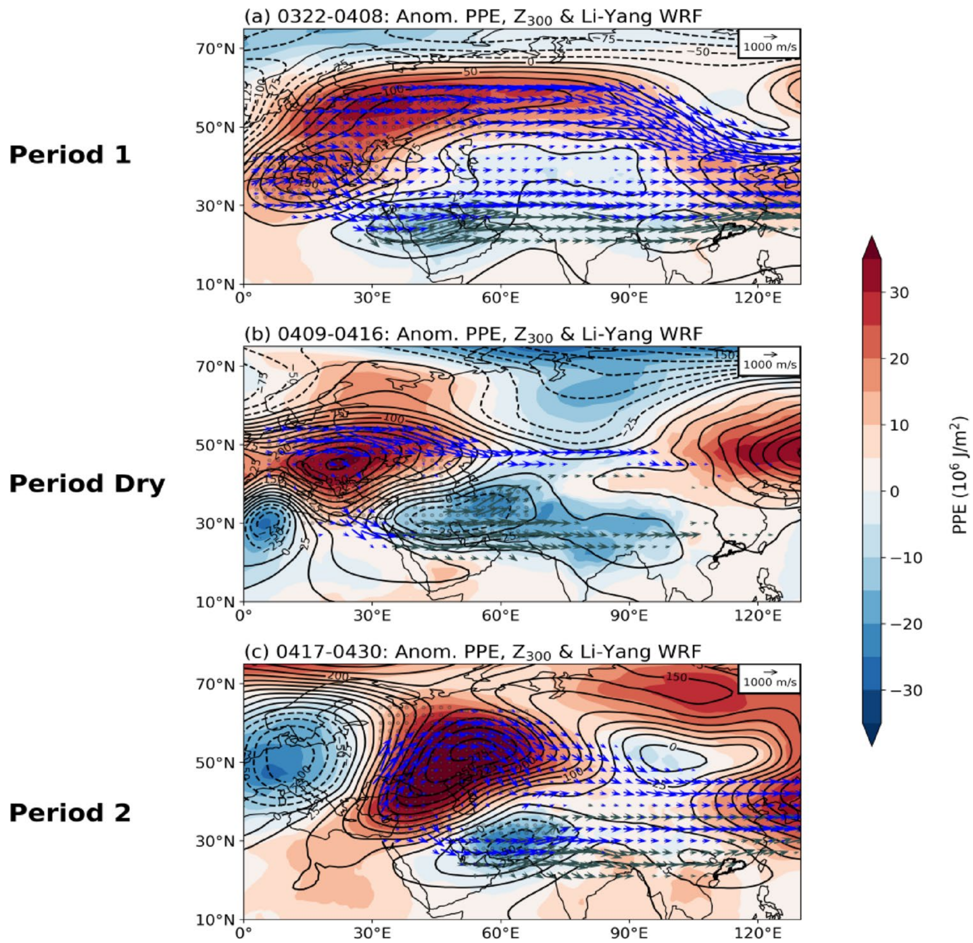

Fig. 4 Mean wave ray fluxes originate from Europe (blue vectors, m s^{-1}) and West Asia (green vectors, m s^{-1}), 300 hPa geopotential height anomalies (contours, gpm) and the PPE anomalies (shading, 10^6 J m^{-2}) during the P1 (**a**), P Dry (**b**) and P2 (**c**), in which the gray dots denote the sources of the wave energy

is quite similar to the circulation in April 2024, which means that the EEWA wave train is a decadal pattern that prevails in early twenty-first century, thus is a long term background. While in 2024 this wave train is extremely amplified.

April mean circulation pattern in Fig. 2a and c shows the spatial connection between the Eastern Europe high PPE and upper-level divergence over Guangdong that plays an important role in extreme precipitation. We further calculated the daily precipitation index by averaging the precipitation over all stations within Guangdong Province (illustrated by heavy black line in Fig. 2a). Figure 3 shows that the first extreme precipitation event occurs in early April (April 3–8). And the remaining three events are concentrated in mid-to-late April (April 17–May 1) after a nearly one-week no rain interval in mid-April (April 9–16, the dry Period). However, the intervals between the three precipitation peaks in mid-to-late April are short (1–2 days), which may be considered as one continuous varying precipitation process. So, daily variabilities of the April extreme precipitation show two time-scales, the low frequency part with two separated processes in one month (a time scale of nearly 2 weeks), and a typical time scale may be connected to planetary scale circulations. And the high frequency part, that is the variabilities within the two processes, indicates a period less than one week, which is connected with local synoptic or other smaller scale systems.

Since the high PPE over Eastern Europe and circulation near Guangdong is connected by the EEWA wave train, the time series of Eastern Europe PPE (EEPPE, the PPE averaging over the Eastern Europe enclosed by the blue rectangle in Fig. 1b) is low-passed to show only the low frequency part that connected to the planetary scale variation (Fig. 3). The EEPPE increases more than 2 weeks before and reaches its maximum on March 30 nearly one week before the first Guangdong precipitation process at the beginning of April with its peak on April 5. Then the EEPPE keeps in a high value in April that is accompanied by intermittent extreme rains in Guangdong. As the EEPPE decays in the ending week of April, the Guangdong precipitation decays. Comparing the time series of the EEPPE and the Guangdong precipitation, it is shown that the low-frequency evolution of the precipitation in Guangdong is highly consistent with the 7-day running averaged regional-mean variation of the EEPPE, with the latter leading the former by more than one week. This confirms that the variation of the EEPPE serves

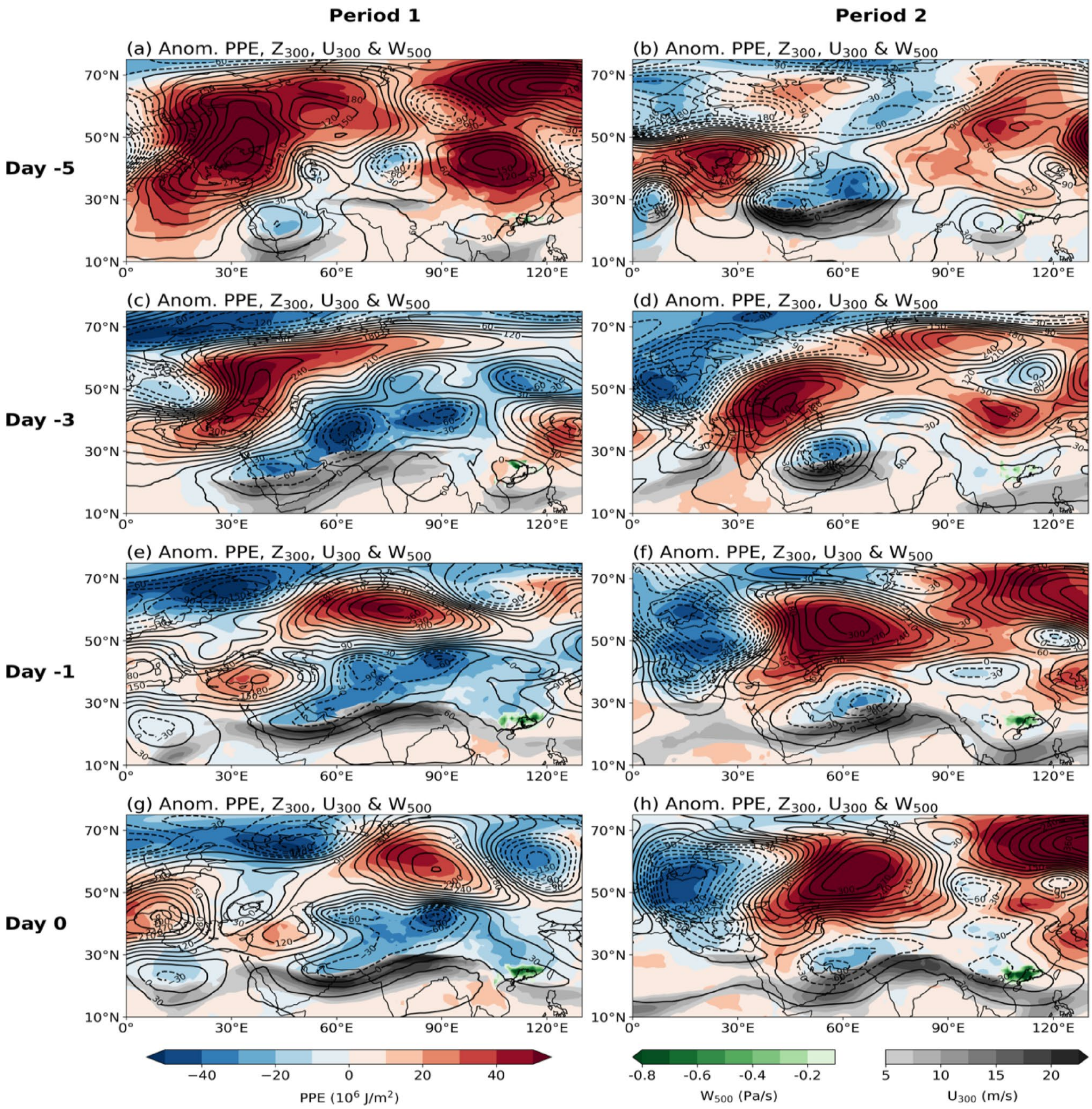

Fig. 5 Anomalous PPE (color shading, 10^6 J m^{-2}), 300 hPa geopotential height (contours, gpm), 300 hPa zonal wind (grey shading, m s^{-1}), and 500 hPa vertical velocity near Guangdong (green shading, Pa s^{-1}) for day −5 (**a** and **b**), day −3 (**c** and **d**), day −1 (**e** and **f**) and day 0 (**g** and **h**) in the P1(**a**, **c**, **e** and **g**) and P2 (**b**, **d**, **f** and **h**)

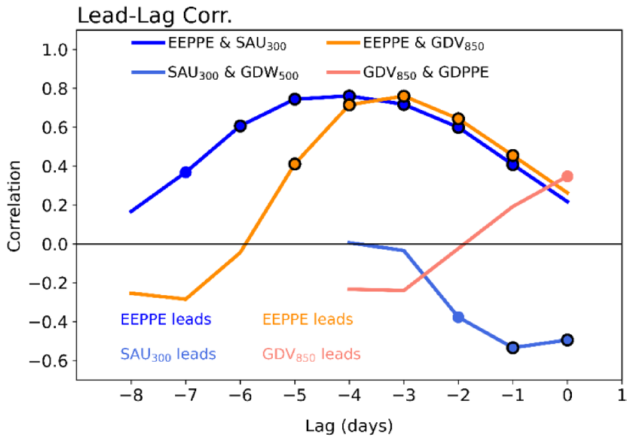

Fig. 6 Lead-lag correlations between the daily variabilities of: the EEPPE and 300 hPa zonal wind over West Asia (SAU_{300}, the mean 300 hPa zonal wind velocities averaging over the area enclosed by the blue box in Fig. 2c, deep blue line), the SAU_{300} and the 500 hPa vertical velocity averaging over Guangdong (GDW_{500}, light blue line), the EEPPE and the amplitude of southerly wind to Guangdong (GDV_{850}, 850 hPa meridional wind amplitudes averaging along the red line in Fig. 7a, orange line), and the GDV_{850} and regional mean PPE anomalies over Guangdong (GDPPE, pink line), dotes/black circled dotes denotes significant values at the 95%/99% confidence levels

as a low frequency modulation on the Guangdong precipitation through the planetary scale wave train.

3.3 Mechanism of Eastern Europe high PPE influencing extreme precipitation in Guangdong through the EEWA wave train.

3.3.1 Wave energy propagation in the two precipitation periods

The April mean circulation and Li-Yang WRF distribution shown in Sect. 3.2 indicated a connection between the extreme high temperature in Europe and upper troposphere circulation near Guangdong. To look further into how this connection forms during the temporal-spatial variation process, we calculate the period mean wave ray flux (Li-Yang WRF) (Yang et al. 2025) and the corresponding geopotential height and PPE anomalies over the periods from March 22 to April 8 (P1), and from April 17 to April 30 (P2) respectively (Fig. 4a and c). Both in the P1 and P2, the positive PPE anomalies expand from northern to southern Eastern Europe with the high PPE zone located more eastward in P2 than in P1. In P1, the Li-Yang WRF show the wave energy originated over northern Eastern Europe goes eastward mainly along the subpolar wave guide. The continuously

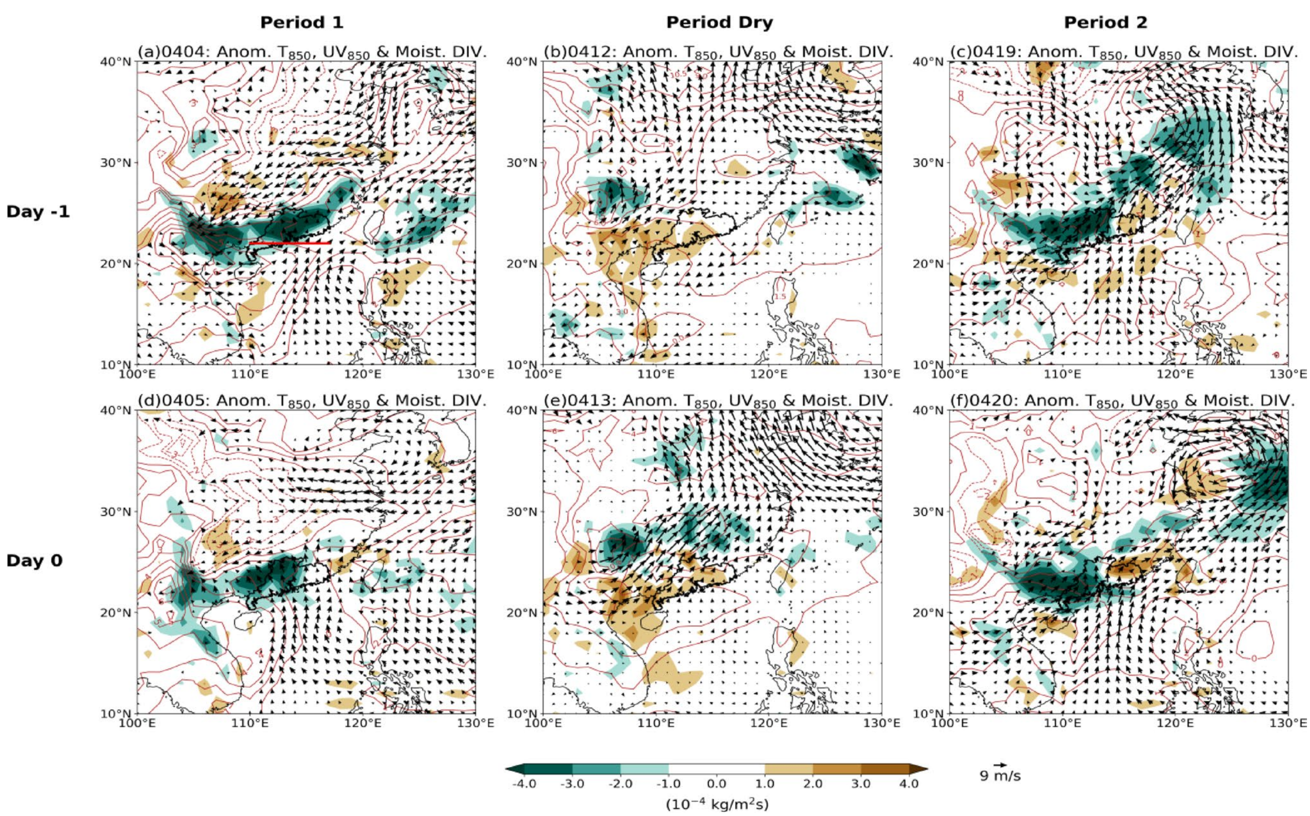

Fig. 7 Vertically integrated (1000–850 hPa) moisture flux divergence anomalies (shading, 10^{-4} kg m^{-2} s^{-1}), 850 hPa temperature anomalies (contours, °C) and wind anomalies (vectors, m s^{-1}) for Day − 1 (**a**–**c**) and Day 0 (**d**–**f**) in the P1 (**a**, **d**), P Dry (**b**, **e**) and P2 (**c**, **f**)

downstream propagations of the Li-Yang WRF lead to existence of wave train along the Li-Yang WRF path at high latitudes. However, the Li-Yang WRF originated at southern Eastern Europe go southeastward to West Asia, major of which is obstructed by the Tibetan Plateau and show a convergence of the Li-Yang WRF west of the Tibetan Plateau, eventually leads to an existence of the West Asia low. The other part of the Li-Yang WRF go further eastward along north of the Tibetan Plateau to Guangdong and contribute to the shaping of the low-pressure center there. The quasi-stationary West Asia low action center can act as a secondary wave source that relays the origin high PPE induced wave source in Eastern Europe. So, we further calculate the Li-Yang WRF from the West Asia low (gray green vectors in Fig. 4a and b), which show wave energy paths along both the south and north of the Tibetan Plateau to Guangdong and leads to a downstream low pressure center there. Therefore, the development of the low-pressure anomaly near Guangdong is the result of both the wave energy directly from Eastern Europe and that from the wave action center at West Asia. The PPE distribution and the Li-Yang WRF path in P2 are similar to that in P1. However, due to the continuous propagation of the wave energy, both the Eastern Europe and the West Asia wave action center intensify and move slightly eastward in P2 but still trapped at west of the Ural Mountains and the Tibetan Plateau. While, the waves rapidly develop downstream both along near 50°N and 30°N. As a conclusion, the period mean Li-Yang WRF further reveals the sub-month variation between the two extreme rain periods, illustrating how the wave energy from Eastern Europe induces the development of the West Asia low which then acts as a second wave energy source and how the low-pressure center near Guangdong develops.

To complete the picture of the planetary-scale circulation adjustment in April, we also computed the 7-day mean 300 hPa circulation and the Li-Yang WRF vectors for the no-rain period (April 9–16). The results show that during the two rain periods (P1 and P2), large perturbed potential energy (PPE) exists over Eastern Europe, accompanied by strengthened downward wave energy propagation (large WRF vectors) and amplified downstream wave action centers including the upper-level trough near Guangdong. In the dry period between P1 and P2 (Fig. 4b), the high-pressure anomaly and PPE over Europe weaken and narrow; correspondingly, the WRF vectors weaken and the wave energy propagation paths shorten, leading to a retreat of the eastern edge of the South Asian low-pressure band and the appearance of a weak ridge over Guangdong. Thus, owing to the variability of PPE over Europe, the upper-level planetary-scale waves exhibit a developing-decaying-developing process in April.

3.3.2 Mechanism revealed by the daily variabilities

The PPE, 300 hPa geopotential height anomalies, and westerly jet accompanying the Asia low on the 5, 3, 1, 0 days preceding (denoted as the day −5, day −3, day −1 and day 0) the maximum precipitation in P1 and P2 are then further pictured respectively in Fig. 5 to show how upper troposphere large scale circulations evolve and how the teleconnection between the Europe high PPE and local circulations corresponding to Guangdong extreme precipitation forms day by day based on the wave energy connection shown in the above.

The evolutions of circulation corresponding to the proceeding days of the two extreme precipitation periods show much similarities. Accompanying the continuous downstream wave energy propagation, the positive geopotential height and PPE anomalies over the Eastern Europe decay and go eastward in P1, and the negative geopotential height and PPE anomalies develop over West Asia and downstream regions continuously. Accompanying the developing of the low-pressure centers, the westerly jet intensifies gradually which is accompanied by a gradually intensification of an upper-level divergence zone over Guangdong.

The rain-stop period from April 9 to April 16 separate the two extreme precipitation processes, which makes the evolution of the two processes show much independence. The similarity of the two synoptic evolution process confirms that they are under the control of a quasi-stable background, that is, the whole April precipitation is under the influence of the EEPPE through the EEWA wave train, which is both indicated by the spatial circulation pattern and temporal relationship between the EEPPE index and the GDP index (Figs. 3 and 4). However, they are not isolated, the later process is still shown to be connected with the earlier process through the down-stream wave energy propagation. Figure 4 shows that the PPE anomalies and the corresponding Li-Yang WRF are stronger in the P1 than P2. During the early developing days of the P1, the West Asia low amplifies gradually as the wave energy continuously converges there, after that the EEWA wave train forms. Whereas, for the P2, since the EEWA wave train has formed during the P1, the influence of the variability of PPE over Eastern Europe on the circulation related with the precipitation over Guangdong would be faster. This explains why the EEPPE index leads the GDP index longer in the P1 than in the P2 (Fig. 3). Moreover, the Li-Yang WRF indicates that wave energy propagations are along both the subtropical and subpolar wave guides (Fig. 4). So, the Eastern Europe high also varies both in the amplitude and location.

To show how the connection between the EEPPE and the Guangdong precipitation constructs, we further calculate the daily indices of the south Asia jet (SAU_{300}, the mean 300 hPa zonal wind velocities averaging over the area enclosed by the blue box in Fig. 2c, which covers the core of the South Asian westerly jet, lies exactly at the southern periphery of the Tibetan Plateau, and represents the dynamically sensitive region with the most concentrated positive zonal wind anomalies), the vertical velocity and the PPE over Guangdong (GDW_{500} and GDPPE, 500 hPa vertical velocity and PPE averaging over Guangdong Province), and the amplitude of southerly wind to Guangdong (GDV_{850}, 850 hPa meridional wind amplitudes averaging along the red line in Fig. 7a) in the period from March 15 to May 2. Based on these daily indices, the lead–lag correlations between the EEPPE and the SAU_{300}, the SAU_{300} and the GDW_{500}, the EEPPE and the GDV_{850}, and the GDV_{850} and the GDPPE are calculated (Fig. 6).

The correlations indicate the EEPPE has a maximum leading of 6 days and 5 days for the SAU_{300} and GDV_{850}. This is consistent with the time scale of the wave energy propagation from Eastern Europe to the vicinity of Guangdong along north of the Tibetan Plateau (Figs. 2b and 4). Moreover, the EEPPE leads the SAU_{300} longer than the GDV_{850}. This may be associated with the factor that the wave energy can reaches southeast China directly, while, the EEPPE influence the SAU_{300} through energy propagation route along south of the Tibetan Plateau, involving the relay effect of the West Asian low-pressure center thus taking a longer time (Figs. 2b and 4). Furthermore, the variabilities of GDV_{850} and GDPPE show a significant correlation when the former leads by 0–1 day. This suggests that local GDPPE intensifies almost immediately as the 850 hPa circulation strengthens, due to the key role of warm advection in modulating PPE (Li et al. 2023). Meanwhile, the enhancement of SAU_{300} leads the intensification of local vertical velocities for 1 day indicating a fast response of air rising to jet variabilities. The intensification of air rising contributes not only to precipitation increase but also to the conversion of PPE into kinetic energy. Therefore, the EEPPE influence the local dynamic condition through two paths. One modulates the upper troposphere jet in a direct dynamic path. The other influence the local GDPPE through thermal advection that induced by variability of local horizontal velocity field. So, the EEWA wave train serves as a planetary scale modulator.

3.3.3 Low level conditions for extreme precipitation

To investigate how the upper-level EEWA wave train dynamically modulates the local thermodynamic environment for the extreme precipitation over Guangdong, the low-level circulations and moisture convergence on day −1 and day 0 in P1 and P2 are shown in Fig. 7.

Comparing Figs. 5 and 7, the velocity fields present a typical baroclinic frontal cyclone structure (Holton and Hakim 2013). Specifically, the 850 hPa wind vectors show a cyclonic circulation around Guangdong, located directly beneath the 300 hPa low-pressure anomaly center. It is crucial to note that the development of this low-level cyclone is not an isolated event; rather, it is a direct dynamic response to the upper-level divergence field induced by the downstream propagation of the EEWA wave train at the jet exit zone (Figs. 2c and 5).

Driven by this coupled cyclonic circulation, the cold, dry northerly winds from the continent converge with the warm, moist southerly winds from the ocean, forming a distinct moisture convergence zone along the temperature front. This intense low-level thermal advection and moisture convergence, mechanically forced by the upper-level wave train, play an essential role in the rapid accumulation of local PPE over South China. With the continuous assistance of upper-level divergence, the vertical motion is further enhanced, establishing a high-low level coupled dynamic structure that perfectly translates the remote planetary wave forcing into optimal local conditions for extreme precipitation.

Conversely, during the dry period, as the upper-level trough retreats westward (Fig. 4), the 850 hPa cyclonic circulation and the associated cold/warm fronts completely disappear, leading to the cessation of rainfall over Guangdong. The contrast between the precipitating and non-precipitating periods further demonstrates that the temporal evolution of the low-level circulation and moisture transport is strictly consistent with the modulation of the upper-level planetary waves.

3.4 Relationship between local energy transform and extreme precipitation

The above section revealed that the PPE and vertical velocities over Guangdong can be influenced by the increase of the PPE over Eastern Europe about one week before. In this section we discuss how these local dynamic conditions are connected with the occurrence of extreme precipitation. Figures 1a and 8 show that the rank 1st April precipitation is accompanied by the rank 1st PCpe (PCpe is negative), which indicates that the extreme precipitation can be attributed to the extremely large transformation of the PPE to kinetic energy (Zhang et al. 2023). To investigate how the PCpe increases and contributes to extreme precipitation, we show the daily variabilities of the precipitation and the vertical sections of the PPE and PCpe averaging over the precipitation region in Guangdong (GDPPE and GDPCpe) from 27 March to 2 May 2024 (Fig. 9).

The GDPPE keeps positive at upper and lower troposphere for 3–4 days before the beginning of the first precipitation period (April 4–8) (Fig. 9). During these days, the GDPCpe shows weak positive above 850 hPa (solid black

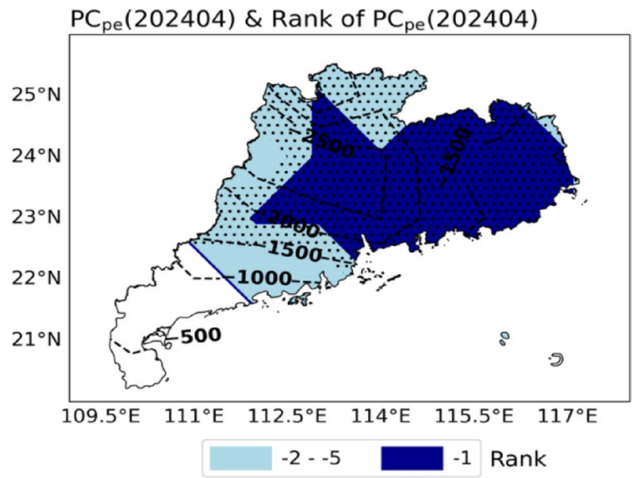

Fig. 8 The PCpe anomalies (contours, W m^{-2}) with its ranking (color shading) over Guangdong in April 2024, where the stippled areas denote above the 99% confidence levels

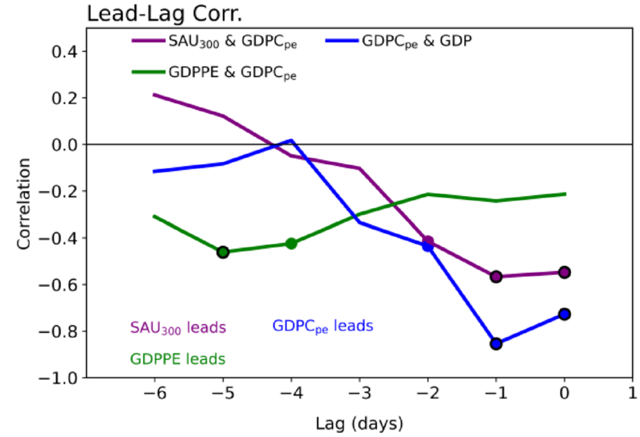

Fig. 10 Lead-lag correlations between the daily variabilities of: the SAU_{300} and the PCpe over Guangdong (GDPCpe, purple line), GDPPE and GDPCpe (green line), and GDPCpe and precipitation anomalies over Guangdong (GDP, blue line). Dotes/black circled dotes denotes significant values at the 95%/99% confidence levels

contours in Fig. 9). As the GDPCpe transiting from positive to negative (dashed black contours in Fig. 9), indicating the transition from potential energy to kinetic energy, the precipitation begins. And the precipitation increases with the amplification of the negative GDPCpe. Meanwhile, the intensifying of negative GDPCpe is accompanied by the gradual decreases of the GDPPE from strong positive to negative. Therefore, the acceleration of velocity field is a result of transition of GDPPE to kinetic energy.

As the GDPPE keeps a negative value from surface to the upper troposphere for nearly one week, no precipitation occurs. After that, the GDPPE re-increase 4–5 days before the beginning of the second precipitation process (April 17–30). However, the second precipitation process persists longer and is accompanied by a longer persistence of local positive GDPPE, which is composed of three sub-cycles with short temporal intervals between the precipitation peaks. In the evolutions of the second precipitation process, the energy evolution and transition are similar to the first precipitation process. The above discussion shows that the increase of precipitation is a result of the transition of the local strong GDPPE to kinetic energy, which is modulated by the variation of the PPE over Eastern Europe as indicated by the results in Figs. 3, 4, 5, and 6. The GDPPE leads the GDPCpe for a longer period of 4–5 days (Fig. 10), which indicates that relationship between the GDPPE and the GDPCpe involves more complex process, that the PPE may accumulate till a suitable dynamic condition trigger the conversion from the PPE to kinetic energy. To show the role the south Asia jet acted in the precipitation process, we further calculate the lead-lag correlations between the precipitation,

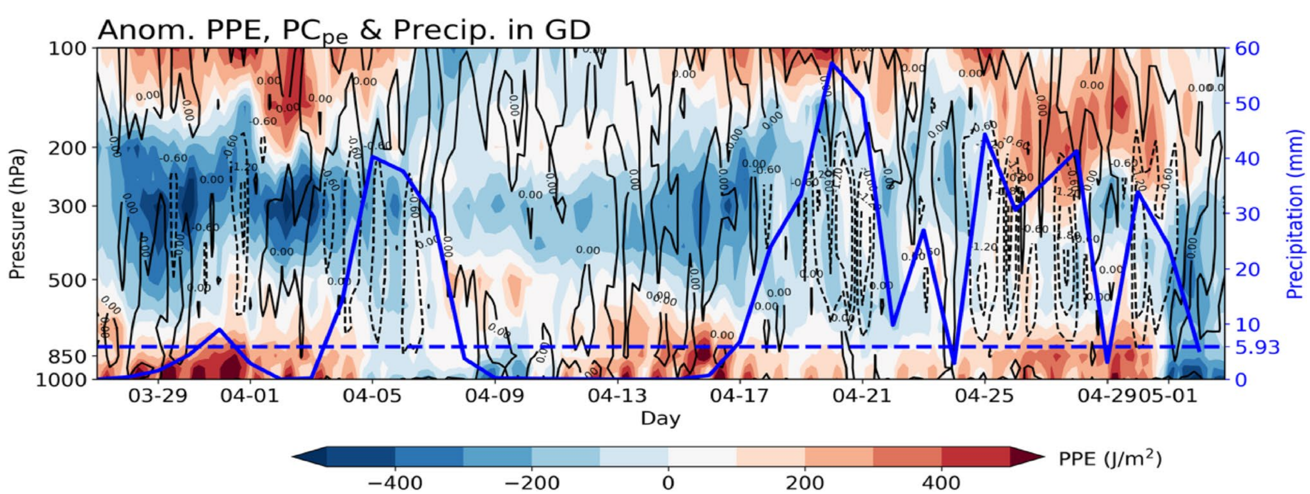

Fig. 9 Vertical section of the daily variation of the PPE (shading, J m^{-2}) and the PCpe (contours, W m^{-2}) from 27 March to 2 May 2024, with the blue line being the daily variabilities of the precipitation (blue line, mm) over Guangdong, the blue dashed lines indicating the climatological mean daily precipitation

the SAU_{300}, and the GDPCpe. The GDPCpe/SAU_{300} is most significant correlate with the precipitation/GDPCpe when the former leads by 0–1 day, which indicates that precipitation is an immediate result of the decrease of the GDPCpe, and the increase of the south Asia jet also has a fast influence on the GDPCpe by inducing air rising. Therefore, the GDPPE, GDPCpe and the south Asia jet construct a local thermal-dynamic system which varies in a transient time scale.

4 Conclusion and discussions

4.1 Conclusion

We discussed the extremeness of the April precipitation in 2024 in the Guangdong Province and the possible cause. The RAM attributes the Guangdong extreme precipitation to the extreme strong local PPE-kinetic energy transition, and the remote extreme high temperature in Eastern Europe (Figs. 1a, b, and 8). Further investigations explain how the remote extreme high temperature and PPE in Eastern Europe and the high temperature surrounding Guangdong jointly influence the extreme precipitation in April by tracing wave energy propagation, large scale circulation evolution, and local PPE-kinetic energy conversion processes. The EEWA wave train occurred in April 2024 is an extreme amplification of the long term background wave train pattern that exists in recent two decades (Figs. 1c and 2d). The persistent extreme high temperature in April 2024 in Eastern Europe is accompanied by anomaly high PPE and high-pressure anomaly center, which act as a Rossby wave energy source. The wave energy go southeastward from Eastern Europe to West Asia then go further eastward around the Qinghai-Tibet Plateau, in which the development of the West Asia low acts as a second wave energy source. The downstream propagation of wave energy maintains the EEWA wave train and the south Asia westerly jet upstream of the Guangdong Province (Figs. 2a–c and 4). the EEWA wave train acts as a planetary scale modulator (Figs. 3, 4, 5, 6, and 7) and influences the local thermal-dynamic process in Guangdong through two paths (Figs. 5, 6, and 7). In the direct path it leads to the variability of westerly jet above Guangdong that influence the vertical velocity directly. In the indirect path, it also impacts the local PPE by modulating the local thermal advection. The local energetic analysis further reveals the local cause of the extreme precipitation in Guangdong. The increase of precipitation is a result of the transition of the local PPE to kinetic energy which is triggered by upper troposphere jet-induced air rising. The local PPE, PCpe and the south Asia jet construct a local thermal-dynamic system which varies in a transient time scale. While this local thermal-dynamic system is modulated by the low frequency variabilities of the remote PPE in Eastern Europe.

Based on the investigation in this study, the occurrence of the long-lasting April extreme precipitation is under the contral of the joint influence of the EEWA wave train induced by remote extreme heat and local thermodynamic processes. The former acts as a slow modulator and long-leading precursor, while the latter shows a transient reaction to local dynamic, heat, and moisture conditions. As synthesized in the schematic diagram (Fig. 13), this comprehensive physical mechanism can be explicitly summarized into two main stages. (1) Remote Influence: The buildup of perturbation potential energy over the extreme heat in Eastern Europe acts as a wave source, sustaining the quasi-stationary EEWA wave train. The downstream propagation of this wave train intensifies the South Asia westerly jet and the frontal cyclone near Guangdong, which in turn enhances moisture and heat transport from the surrounding warm oceans, leading to an increase in local PPE and moisture convergence. (2) Local Intensification: At the jet-exit zone, the upper-level divergence and the warm air ascent at the cyclone front trigger the rapid release of the accumulated local PPE. This process violently accelerates the ascending motion, ultimately resulting in the extreme precipitation over Guangdong.

4.2 Discussion

Since the April 2024 extreme rains in Guangdong are frontal rains (Fig. 7), the intensity of the cold air intruding and warm humidity air transport are both important. The results revealed in this study shows that the influence from the midlatitude circulations have a critical importance. The midlatitude circulations act as one side role of this frontal extreme precipitation in April 2024. The upper troposphere cyclonic circulation at the eastern end of the EEWA wave train transports cold air southeastward and induces intensification of front and emerging of low troposphere cyclone (Fig. 7). It also contributes to the accumulation of local PPE through the low level wind fields. And the EEWA wave train influences the strength of West Asia jet, which triggers the local energy transition, and the release of local PPE (intensification of the PCpe) at the left of the jet-exit zone (Figs. 2a and 5). This connection structured by the EEWA wave train explains why the extremeness of the April 2024 precipitation in Guangdong can be attributed to the extremeness of Eastern Europe high temperature and local PCpe. Moreover, the EEWA wave train that connects the remote PPE anomalies and the local circulation in Guangdong makes the variation of the PPE in Eastern Europe an intraseasonal scale precursor for the occurrence of extreme precipitation in Guangdong. The existence of the EEWA wave train also implies a decadal-scale background state that enables the

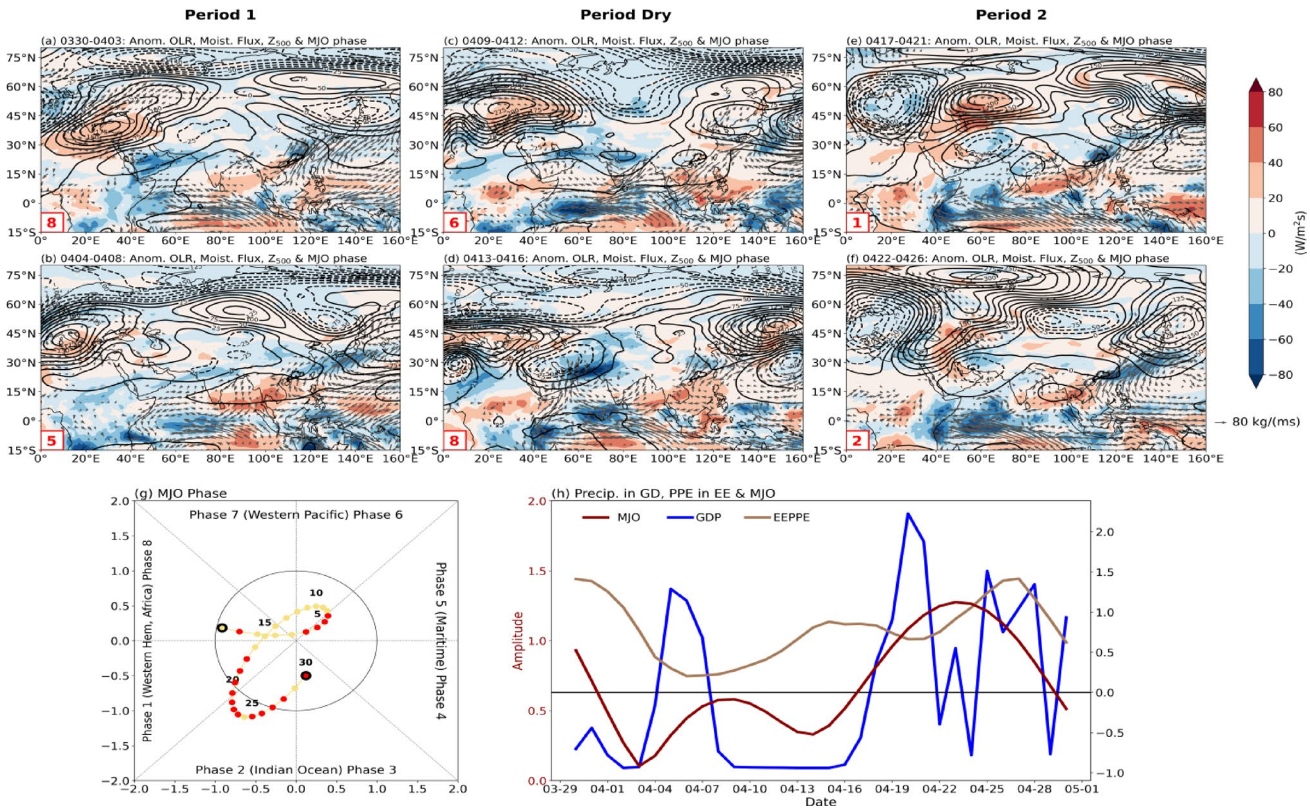

Fig. 11 Anomalous OLR (shading, W m^{-2}), 500 hPa geopotential height (contours, gpm), vertically integrated (1000–850 hPa) moisture flux (vectors, kg m^{-1} s^{-1}) and MJO phase in the P1 (**a** and **b**), P Dry (**c** and **d**) and P2 (**e** and **f**); **g** MJO phase from 30 March to 30 April 2024. Black-bordered dots mark the start (30 March) and end (30 April) dates. Red dots indicate days with daily precipitation exceeding 5 mm; and (h) normalized 7-day running mean Eastern Europe PPE anomalies (EEPPE, grey line), Guangdong precipitation (GDP, blue line) and MJO amplitude (dark red line) from March to 30 April 2024

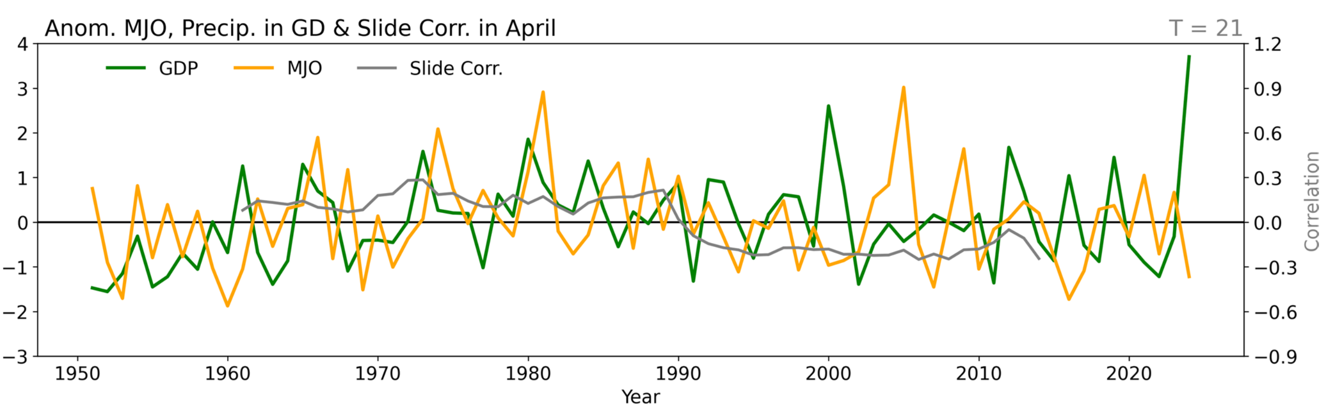

Fig. 12 The normalized indices of the MJO (yellow line), Guangdong precipitation (GDP, green line) and the 21-year running correlation coefficients (grey line) between them

influence of high temperatures in Europe on precipitation in Guangdong.

Warm and moisture air transportations are found to be mostly attributed to Western Pacific Subtropical High and the MJO and can be influenced by SST anomalies over India Ocean and Western tropical Pacific (Ding 1994; Yang and Lau 2004; Wan et al. 2009; Xu et al. 2019; Bai et al. 2011). Zhang et al. (2025) attributed the 2024 April extreme precipitation to the influence of MJO and the anti-cyclonic circulation over the Western North Pacific (ACC). Their study explains the water vapor source for the April 2024 extreme precipitation.

To evaluate the influence of the MJO on the April 2024 extreme precipitation process, the temporal evolution of the MJO phase and intensity are shown in Fig. 11g and h. The multi-day mean 500 hPa geopotential heights, the OLR

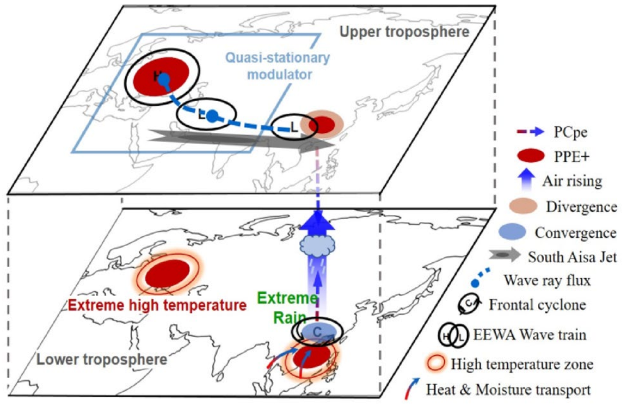

Fig. 13 Schematic Diagram of the Physical Mechanism Linking Extreme High Temperatures in Eastern Europe to Extreme rainfall in Guangdong (GD). (1) Remote Influence: The buildup of perturbation potential energy (PPE+) over the extreme heat in Eastern Europe (EE) acts as a wave source, sustaining the quasi-stationary EEWA wave train. This wave's downstream propagation intensifies the South Asia jet and the frontal cyclone near Guangdong. The cyclone enhances moisture and heat transport from the warm South China Sea and the Bay of Bengal, leading to an increase in local PPE and moisture convergence over Guangdong. (2) Local Intensification: At the jet-exit zone, upper-level divergence and warm air ascent at the cyclone front trigger the release of accumulated local PPE. This accelerates air rising, which results in extreme precipitation over Guangdong

and the moisture flux vectors in the Period 1, Period 2 and Period dry are further illustrated to show the influence of the MJO on the precipitation process in April (Fig. 11a–f). The results show that the April precipitation events are accompanied by the evolution of MJO (Fig. 13g and h). Generally, the MJO can induce anticyclonic/cyclonic circulation to northeast/northwest of the convergence zone. For example, during April 4–8, the MJO is in phase 5. The convergence near the Maritime continent can induce a 850 hPa anticyclonic circulation east of Guangdong, which contributes the moisture transport to Guangdong. However, the upper level (500 hPa) midlatitude trough over Guangdong and anticyclone near Japan also induce southeast flow and moisture transport to Guangdong at 850 hPa (Fig. 11b). So, in this case, both the MJO and the midlatitude upper-level circulation make contribution to the precipitation.

The MJO seems not to be a dominant factor, based on the following reasons. First, nearly half of the precipitation days are connected with the weak and untypical phase MJO (Fig. 11g and h). Second, the similar MJO phases are corresponding to the converse moisture transport pattern (Fig. 11a and d). Finally, the MJO lags the precipitation during the majority of the precipitation days (Fig. 11h) which implies that the MJO might not act as the main cause in many of the precipitation days. However, in the ending week of April, the MJO is intensified and leads the precipitation for two days. The MJO induced convergence in Indian Ocean contributes to the intensifying the moisture transport from South China Sea to Guangdong in this period (Fig. 11f). By contrast, the EEPPE variation lags the precipitation, which implies that the EEPPE involved upper level wave train may not act as the dominant role in the precipitation. However, the upper level trough keeps its location above Guangdong (Fig. 11e and f) during the whole P2 period which provide a persistent dynamic support for the low level cyclone. As both of the two factors decay, the precipitation decays too. Therefore, in this period, the precipitation is a result of the joint impacts of the MJO and the upper level wave train, in which the MJO is more important. Furthermore, Fig. 11 show that, the intensity of the MJO in April 2024 is very weak compared with other years in the period 1950–2024. So, the MJO does not contribute the extremeness of the April 2024 precipitation in Guangdong. As a contrast, the air temperature over east Europe reaches the highest in the period 1950–2024. According to the above discussion, we can draw a conclusion that, the MJO contributes to the extreme April 2024 precipitation in Guangdong but the midlatitude wave train (the EEWA wave train) plays a more important role.

Through the perspective of the PPE, our study reveals a physically consistent chain from remote PPE generation, EEWA wave-train maintenance, and South Asian jet enhancement to local PPE accumulation and subsequent PPE-to-kinetic-energy conversion thus make a further understanding of the dynamic and energetic processes underlying the extremeness of the April 2024 precipitation in Guangdong. This study also reveals the unprecedented Eastern European heat anomaly as a key upstream forcing source. These findings suggest that remote Eurasian thermal anomalies can serve as valuable intraseasonal precursors for extreme spring rainfall in South China and provide a new framework for understanding and predicting compound climate extremes across Eurasia.

Furthermore, it is important to place this "Hot-flood teleconnection" within the context of ongoing global climate change. Our sliding correlation analysis demonstrates that the significant positive teleconnection between Eastern Europe and Guangdong has persisted robustly over the past two decades. Under the background of global warming, if no abrupt decadal phase shift occurs to alter the current circulation regime, the continuous and accelerated warming over Eastern Europe is expected to inject greater perturbation potential energy (PPE) into the atmosphere. Such an amplified upstream thermal wave source could potentially increase the intensity and frequency of the EEWA wave train, thereby exerting an even more profound and destructive impact on extreme precipitation in South China. Therefore, utilizing CMIP6 multi-model datasets to project the future evolution trends of this teleconnection mechanism under different warming scenarios represents a highly essential direction for our future research.

Acknowledgements This work is supported by National Key Basic Research Project of China (Grant 2023YFF0805101), National Natural Science Foundation of China (NSFC) Project (42075025) and Laoshan Laboratory (No. LSKJ202202600). We are grateful to all the data providers.

Author contributions Yina Diao and Jianping Li designed the main idea of the study. All authors contributed to the data collection and analysis, as well as graphical analysis and visualization. The first draft of the manuscript was written by Yina Diao and Xinning Zhang. All authors commented on previous versions of the manuscript. All authors read and approved the final manuscript.

Funding This study was jointly sponsored by the National Key Basic Research Project of China (Grant 2023YFF0805101), National Natural Science Foundation of China (NSFC) Project (42075025), Laoshan Laboratory (No. LSKJ202202600) and Fundamental Research Funds for the Central Universities (202242001, 202515028).

Data availability The European Centre for Medium-Range Weather Forecasts (ECMWF) Reanalysis version 5 (ERA5) is available at https://cds.climate.copernicus.eu/datasets/reanalysis-era5-pressure-levels?tab=download; https://cds.climate.copernicus.eu/datasets/derived-era5-pressure-levels-daily-statistics?tab=download; https://cds.climate.copernicus.eu/datasets/reanalysis-era5-pressure-levels-monthly-means?tab=download. The rainfall observations can be obtained from http://data.cma.cn/en/?r=data/detail&dataCode=A.0012.0001.

Declarations

Conflict of interest The authors have no relevant financial or nonfinancial interests to disclose.

References

Andrews DG, McIntyre ME (1976) Planetary waves in horizontal and vertical shear: the generalized Eliassen-Palm relation and the mean zonal acceleration. J Atmos Sci 33:2031–2048. https://doi.org/10.1175/1520-0469(1976)033%3c2031:PWIHAV%3e2.0.CO;2

Bai XX, Li CY, Tan YK et al (2011) Analysis of the Madden-Julian Oscillation impacts on the spring rainfall in east China. J Trop Meteor 27:814–822. https://doi.org/10.3969/j.issn.1004-4965.2011.06.004

Chen YRX, Luo YL (2018) Analysis of paths and sources of moisture for the South China rainfall during the presummer rainy season of 1979–2014. J Meteorol Res 32:744–757. https://doi.org/10.1007/s13351-018-8069-7

Chen XC, Zhao K, Xue M et al (2015) Radar-observed diurnal cycle and propagation of convection over the Pearl River Delta during Mei-Yu season. J Geophys Res 120:12557–12575. https://doi.org/10.1002/2015JD023872

Chen XC, Zhang FQ, Zhao K (2016) Diurnal variations of the land–sea breeze and its related precipitation over South China. J Atmos Sci 73:4793–4815. https://doi.org/10.1175/JAS-D-16-0106.1

Chi Y, He J, Wu Z (2005) Features analysis of the different precipitation periods in the pre-flood season in South China. J Nanjing Inst Meteorol 28:163–171

Ding YH (1992) Summer monsoon rainfalls in China. J Meteorol Soc Jpn 70:373–396. https://doi.org/10.2151/jmsj1965.70.1B_373

Ding YH (1994) Monsoons over China. Kluwer Academic Publishers, Dordrecht, p 419

Ding YH, Wang ZY (2008) A study of rainy seasons in China. Meteorol Atmos Phys 100:121–138. https://doi.org/10.1007/s00703-008-0299-2

Edmon HJ, Hoskins BJ, McIntyre ME (1980) Eliassen-Palm cross sections for the troposphere. J Atmos Sci 37:2600–2616. https://doi.org/10.1175/1520-0469(1980)037%3c2600:EPCSFT%3e2.0.CO;2

Eliassen A, Palm E (1961) On the transfer of energy in stationary mountain waves. Geofys Publ 22:1–23

Euler L (1757) Principes généraux du mouvement des fluides. Mémoires de l'académie des sciences de Berlin 274–315

Fang Y, Chen W, Zhou W (2012) Analysis of the role played by circulation in the persistent precipitation over South China in June 2010. Adv Atmos Sci 29:769–781. https://doi.org/10.1007/s00376-012-2018-7

Gao L, Li JP (2013) Impacts and mechanism of diabatic heating on atmospheric perturbation potential energy. Chin J Geophys 56:3255–3269

Gao L, Huang J, Chen X et al (2017) Risk of extreme precipitation under nonstationarity conditions during the second flood season in the Southeastern Coastal Region of China. J Hydrometeor 18:669–681. https://doi.org/10.1175/JHM-D-16-0119.1

Gao L (2006) Theoretical studies and diagnostic analyses of perturbation potential energy. Ph.D. dissertation, Institute of Atmospheric physics, Chinese Academy of Sciences 138

Gu W, Wang L, Hu ZZ et al (2018) Interannual variations of the first rainy season precipitation over South China. J Clim 31:623–640. https://doi.org/10.1175/JCLI-D-17-0284.1

Hersbach H, Bell B, Berrisford P, Biavati G, Horányi A, Muñoz Sabater J, Nicolas J, Peubey C, Radu R, Rozum I, Schepers D, Simmons A, Soci C, Dee D, Thépaut J-N (2023) ERA5 monthly averaged data on pressure levels from 1940 to present. Copernicus Climate Change Service (C3S) Climate Data Store (CDS). https://doi.org/10.24381/cds.6860a573

Holton JR, Hakim GR (2013) An introduction to dynamic meteorology, 4th ed. Elsevier Academic. https://doi.org/10.1016/C2009-0-63394-8

Huang YJ, Liu YB, Liu YW et al (2019) Mechanisms for a record-breaking rainfall in the Coastal Metropolitan City of Guangzhou, China: observation analysis and nested very large eddy simulation with the WRF model. J Geophys Res 124:1370–1391. https://doi.org/10.1029/2018JD029668

Huyan LD, Li JP, Zhao S et al (2017) The impact of layer perturbation potential energy on the East Asian summer monsoon. J Clim 30:7087–7103. https://doi.org/10.1175/JCLI-D-16-0729.1

Jia XJ, Cao DR, Ge WJ et al (2018) Interdecadal change of the impact of Eurasian snow on spring precipitation over Southern China. J Geophys Res 123:10092–10108. https://doi.org/10.1029/2018JD028612

Jiang ZN, Zhang DL, Xia RD et al (2017) Diurnal variations of presummer rainfall over Southern China. J Clim 30:755–773. https://doi.org/10.1175/JCLI-D-15-0666.1

Karoly DJ (1983) Rossby wave propagation in a barotropic atmosphere. Dyn Atmos Oceans 7:111–125. https://doi.org/10.1016/0377-0265(83)90013-1

Lagrange JL (1853) Mécanique analytique, vol vol 1. Mallet-Bachelier

Li JP, Gao L (2006) Theory on perturbation potential energy and its applications-concept, expression and spatio-temporal structures of perturbation potential energy. Chin J Atmos Sci 30:834

Li YJ, Li JP (2012) Propagation of planetary waves in the horizontal non-uniform basic f low. Chin J Geophys 55:361–371. https://doi.org/10.6038/j.issn.0001-5733.2012.02.001

Li L, Nathan TR (1997) Effects of low-frequency tropical forcing on intraseasonal tropical–extratropical interactions. J Atmos Sci 54:332–346. https://doi.org/10.1175/1520-0469(1997)054%3c0332:EOLFTF%3e2.0.CO;2
Li YJ, Li JP, Jin FF et al (2015) Interhemispheric propagation of stationary Rossby waves in a horizontally nonuniform background flow. J Atmos Sci 72:3233–3256. https://doi.org/10.1175/JAS-D-14-0239.1
Li YJ, Feng J, Li JP et al (2019) Equatorial windows and barriers for stationary Rossby wave propagation. J Clim 32:6117–6135. https://doi.org/10.1175/JCLI-D-18-0722.1
Li J, Zheng CS, Yang Y et al (2023) Predictability of spatial distribution of pre-summer extreme precipitation days over southern China revealed by the physical-based empirical model. Clim Dyn 61:2299–2316. https://doi.org/10.1007/s00382-023-06681-2
Li XZ, Wang DH, Zhou W (2024) Multiple-time-scale variations of the record-breaking pre-summer rainfall over South China in 2022. J Clim 37:1965–1980. https://doi.org/10.1175/JCLI-D-23-0586.1
Lorenz EN (1955) Available potential energy and the maintenance of the general circulation. Tellus B Chem Phys Meteorol 7:157–167. https://doi.org/10.3402/tellusa.v7i2.8796
Luo YL, Wang H, Zhang RH et al (2013) Comparison of rainfall characteristics and convective properties of monsoon precipitation systems over South China and the Yangtze and Huai River Basin. J Clim 26:110–132. https://doi.org/10.1175/JCLI-D-12-00100.1
Luo YL, Zhang RH et al (2017) The Southern China Monsoon Rainfall Experiment (SCMREX). Bull Am Meteorol Soc 98:999–1013. https://doi.org/10.1175/BAMS-D-15-00235.1
Ma W, Huang W, Yang Z et al (2018) Dynamic and thermodynamic factors associated with different precipitation regimes over south China during pre-monsoon season. Atmosphere. https://doi.org/10.3390/atmos9060219
Miao R, Wen M, Zhang RH et al (2019) The influence of wave trains in mid-high latitudes on persistent heavy rain during the first rainy season over South China. Clim Dyn 53:2949–2968. https://doi.org/10.1007/s00382-019-04670-y
Plumb RA (1985) On the three-dimensional propagation of stationary waves. J Atmos Sci 42:217–229. https://doi.org/10.1175/1520-0469(1985)042%3c0217:OTTDPO%3e2.0.CO;2
Qiu D, Yao SX, Xia YC (2022) Pre-summer persistent heavy rain over southern China and its relationship with intra-seasonal oscillation of tropical atmosphere. J Trop Meteor 28:445–456
Ren LW, Zhou TJ, Zhang WX (2020) Attribution of the record-breaking heat event over Northeast Asia in summer 2018: the role of circulation. Environ Res Lett 15:054018. https://doi.org/10.1088/1748-9326/ab8032
Rivière G, Joly A (2006a) Role of the low-frequency deformation field on the explosive growth of extratropical cyclones at the jet exit. Part I: barotropic critical region. J Atmos Sci 63:1965–1981. https://doi.org/10.1175/JAS3728.1
Riviere G, Joly A (2006b) Role of the low-frequency deformation field on the explosive growth of extratropical cyclones at the jet exit. Part II: baroclinic critical region. J Atmos Sci 63:1982–1995. https://doi.org/10.1175/JAS3729.1
Schiemann R, Lüthi D, Schär C (2009) Seasonality and interannual variability of the westerly jet in the Tibetan Plateau region. J Clim 22:2940–2957. https://doi.org/10.1175/2008JCLI2625.1
Shao TH, Zhang YC (2012) Influence of winter North Atlantic Oscillation on spring precipitation in China. Plateau Meteor 31:1225–1233
Sun JQ, Ming J, Zhang MQ, Yu S (2018) Circulation features associated with the record-breaking rainfall over South China in June 2017. J Clim 31:7209–7224. https://doi.org/10.1175/JCLI-D-17-0903.1
Sun Y, Li JP, Wang H et al (2023) Extreme rainfall in Northern China in September 2021 tied to air–sea multi-factors. Clim Dyn 60:1987–2001. https://doi.org/10.1007/s00382-022-06439-2
Takaya K, Nakamura H (2001) A formulation of a phase-independent wave-activity flux for stationary and migratory quasigeostrophic eddies on a zonally varying basic flow. J Atmos Sci 58:608–627. https://doi.org/10.1175/1520-0469(2001)058%3c0608:AFOAPI%3e2.0.CO;2
Trenberth KE (1986) An assessment of the impact of transient eddies on the zonal flow during a blocking episode using localized Eliassen-Palm flux diagnostics. J Atmos Sci 43:2070–2087. https://doi.org/10.1175/1520-0469(1986)043%3c2070:AAOTIO%3e2.0.CO;2
Wan RJ, Zhao BK, Wu GX (2009) New evidences on the climatic causes of the formation of the spring persistent rains over southeastern China. Adv Atmos Sci 26:1081–1087. https://doi.org/10.1007/s00376-009-7202-z
Wang B, LinHo ZYS et al (2004) Definition of South China Sea monsoon onset and commencement of the East Asia summer monsoon. J Clim 17:699–710. https://doi.org/10.1175/2932.1
Wang H, Luo YL, Jou BJD (2014a) Initiation, maintenance, and properties of convection in an extreme rainfall event during SCMREX: observational analysis. J Geophys Res 119:13206–13232. https://doi.org/10.1002/2014JD022339
Wang L, Li JP, Wang ZG et al (2014b) The oscillation of the perturbation potential energy between the extratropics and tropics in boreal winter. Atmos Sci Lett 16:119–126. https://doi.org/10.1002/asl2.532
Wang L, Wang ZG, Li JP et al (2015) The impact of extratropics-arctic-seesaw of perturbation potential energy on surface air temperature in boreal winters. Atmos Sci Lett 16:425–431. https://doi.org/10.1002/asl2.575
Wei YY, Huang F, Chen Z (2024) Record-breaking Barents Sea ice loss favors to the unprecedented summertime extreme heatwave in 2021 over western North America by enhancing Rossby wave ridge. Clim Dyn 62:5389–5404. https://doi.org/10.1007/s00382-024-07168-4
Whitham GB (1960) A note on group velocity. J Fluid Mech 9:347–352. https://doi.org/10.1017/S0022112060001158
Wu RG, Kirtman BP (2007) Observed relationship of spring and summer East Asian rainfall with winter and spring Eurasian snow. J Clim 20:1285–1304. https://doi.org/10.1175/JCLI4068.1
Wu MW, Luo YL (2016) Mesoscale observational analysis of lifting mechanism of a warm-sector convective system producing the maximal daily precipitation in China mainland during pre-summer rainy season of 2015. J Meteorol Res 30:719–736. https://doi.org/10.1007/s13351-016-6089-8
Xiao ZX, Duan AM, Chen YH et al (2025) Different mechanisms of Eurasian snow cover on precipitation during the early and late pre-rainy season in South China. Sci China Earth Sci 68:882–897. https://doi.org/10.1007/s11430-024-1490-2
Xie A, Chung YS, Liu X et al (1998) The interannual variations of the summer monsoon onset overthe South China Sea. Theor Appl Climatol 59:201–213. https://doi.org/10.1007/s007040050024
Xu C, Qiao YT, Jian MQ (2019) Interdecadal change in the intensity of interannual variation of spring precipitation over Southern China and possible reasons. J Clim 32:5865–5881. https://doi.org/10.1175/JCLI-D-18-0351.1
Yang FL, Lau KM (2004) Trend and variability of China precipitation in spring and summer: linkage to sea-surface temperatures. Int J Climatol 24:1625–1644. https://doi.org/10.1002/joc.1094
Yang YN, Li JP (2025) Novel monsoon indices based on vector projection and directed angle for measuring the East Asian summer monsoon. Clim Dyn 63:210. https://doi.org/10.1007/s00382-025-07696-7

Yuan F, Wei K, Chen W, Kun FS (2010) Temporal variations of the frontal and monsoon storm rainfall during the first rainy season in South China. Atmos Ocean Sci Lett 3:243–247. https://doi.org/10.1080/16742834.2010.11446876

Zhang MR, Meng ZY (2019) Warm-sector heavy rainfall in Southern China and its WRF simulation evaluation: a low-level-jet perspective. Mon Wea Rev 147:4461–4480. https://doi.org/10.1175/MWR-D-19-0110.1

Zhang YZ, Li JP, Wang QY et al (2019) Variations in atmospheric perturbation potential energy associated with the South China Sea summer monsoon. Clim Dyn 53:2295–2308. https://doi.org/10.1007/s00382-019-04845-7

Zhang YZ, Li JP, Diao YN et al (2023) Energetic connection between the South China Sea summer monsoon and Indian Ocean dipole from the perspective of perturbation potential energy. Clim Dyn 61:2457–2470. https://doi.org/10.1007/s00382-023-06693-y

Zhang LY, Du Y, Zhang YH et al (2025) Extreme rainfall over South China in April 2024 associated with early Indo-Pacific ocean capacitor and MJO events. J Clim 38:3801–3814. https://doi.org/10.1175/JCLI-D-24-0620.1

Zhao S, Li JP, Li YJ (2015) Dynamics of an interhemispheric teleconnection across the critical latitude through a southerly duct during boreal winter. J Clim 28:7437–7456. https://doi.org/10.1175/JCLI-D-14-00425.1

Zhao S, Li JP, Li YJ et al (2019) Interhemispheric influence of Indo-Pacific convection oscillation on Southern Hemisphere rainfall through southward propagation of Rossby waves. Clim Dyn 52:3203–3221. https://doi.org/10.1007/s00382-018-4324-y

Zhao HY, Li JP, Liu Y et al (2024) Multidecadal variability from ocean to atmosphere in the North Atlantic: perturbation potential energy as the bridge. J Clim 37:5187–5206. https://doi.org/10.1175/JCLI-D-24-0025.1

Zuo ZY, Zhang RH, Wu BY (2012) Inter-decadal variations of springtime rainfall over southern China mainland for 1979–2004 and its relationship with Eurasian snow. Sci China Earth Sci 55:271–278. https://doi.org/10.1007/s11430-011-4337-4

Zwack P, Okossi B (1986) A New Method for solving the Quasi-Geostrophic omega equation by incorporating surface pressure tendency data. Mon Wea Rev 114:655–666. https://doi.org/10.1175/1520-0493(1986)114%3C0655:ANMFST%3E2.0.CO;2